2024 European Control Conference (ECC)
June 25-28, 2024. Stockholm, Sweden

Model-based motion control design for the milliAmpere1 prototype ferry

Camilla Fruzzetti[1], Michele Martelli[1], Anastasios Lekkas[2], Roger Skjetne[3], and Morten Breivik[2]

Abstract— **Following the recent upgrade of the propulsion plant configuration for the milliAmpere1 passenger ferry prototype, a model-based controller pipeline suitable for all the milliAmpere1 speed ranges is proposed and evaluated. Some well-known methods for force allocation and reference model systems are implemented together with a nonlinear model-based motion controller, and a comparison study for different combinations is carried out to define the best solution for this application. Considering low-speed operations, the efficiency of three force allocation solutions and three reference models with two possible thruster configurations are investigated. The resulting controllers are evaluated with five performance metrics. For higher-speed operations, a solution with a reference model and a force allocation is presented and investigated. The controllers have been tested via numerical simulations, and based on the performance metrics, indications for the best design options are provided.**

I. INTRODUCTION

Designing an efficient and effective motion control system for a marine surface vessel is a nontrivial task due to the uncertainty involved in calculating the forces and moments acting on the vessel. This challenge can be related to the uncertain nature of the marine environment and the difficulty in accurately modelling the vessel dynamics. For these reasons, motion control of marine surface vessels has been a major topic of interest within ocean engineering for several decades. The first revolutionary works of Elmer Sperry [1] and Nicholas Minorsky [2] took place at the beginning of the XX century, and research on the field has been growing since the 1960s [3].

The resulting literature is wide and includes all types of control engineering methodologies, such as linear and nonlinear control, fuzzy control, (numerical) optimal control and machine learning-based approaches. Naturally, each control methodology is paired with an appropriate modelling framework, including, for instance, first principle approaches (potentially assisted by system identification techniques), model-free control, or neural networks. Some examples can be found in [4], [5], [6], [7], [8], [9], [10], and [11]. The modelling and control methodology selection usually depends on the motion control scenarios considered.

The modelling and control aspects are becoming even more relevant nowadays due to the rise of autonomous surface vehicles (ASVs) and the need for enhanced control systems to perform under limited or zero human intervention. These ASV developments reflect a focus shift within society, where future waterborne transportation is expected to produce almost zero emissions, increase safety, and help decongest traffic by carrying additional cargo and passengers. Several flagship projects in many countries already point to this direction when it comes to cargo [12], [13], whereas the world's first autonomous urban passenger ferry was launched in Stockholm in June 2023 [14].

The milliAmpere1 (mA1) is an autonomous passenger ferry development prototype, which has been used as a test platform in numerous research projects at the Norwegian University of Science and Technology (NTNU) since 2017 [15]. Following a recent modification to mA1, which now becomes equipped with four thrusters instead of two, there is a need to develop a new model and motion control system for the ferry.

The main contributions of this paper revolve around the novel thruster configuration implemented in the ferry and in the comparative evaluation of various combinations of force allocations and reference models. These comparisons aim to establish a suitable motion controller pipeline which effectively controls the motion of the ferry in its entire speed range. Performance metrics are used to evaluate the effectiveness of twelve potential perturbations of the pipeline, along with the assessment of three distinct reference models. The IATE integral metric is, in the end, introduced here to evaluate the actuation error.

The paper is organised as follows. The vessel model adopted is presented in Section II. The general layout of the controllers is shown in Section III, while the components are reported in the following sections: The reference models for both low- and higher-speed ranges in Section VI, the model-based low- and higher-speed controllers in Section IV, and the force allocations for the low- and higher-speed range in Section V. Finally, the simulation results over the entire speed range are given in Section VIII and the Conclusion in Section IX.

II. VESSEL MODEL

To describe the ferry motion in the horizontal plane, it is modelled as a 3-DOF nonlinear system with four actuators.

Based on [16] and taking into account the port-starboard

[1]Camilla Fruzzetti and Michele Martelli are with the Department of Naval Architecture, Electric, Electronic and Telecommunication Engineering (DITEN), University of Genoa, 16145 GENOA, Italy e-mail: camilla.fruzzetti@edu.unige.it, michele.martelli@unige.it

[2] Anastasios Lekkas and Morten Breivik are with the Department of Engineering Cybernetics, Norwegian University of Science and Technology (NTNU), Trondheim, NO-7491 Norway e-mail: anastasios.lekkas@ntnu.no, morten.breivik@ntnu.no

[2] Roger Skjetne is with the Department of Marine Technology, Norwegian University of Science and Technology (NTNU), Trondheim, NO-7491 Norway e-mail: roger.skjetne@ntnu.no

and fore-aft symmetries of mA1, the kinematics and dynamics of the vessel are given in (1) and (2).

$$\dot{\boldsymbol{\eta}} = \mathbf{R}(\psi)\,\boldsymbol{\nu} \tag{1}$$

$$\mathbf{M}\dot{\boldsymbol{\nu}} + \mathbf{C_{RB}}(\boldsymbol{\nu})\boldsymbol{\nu} + \mathbf{C_A}(\boldsymbol{\nu}_R)\boldsymbol{\nu}_R + \mathbf{D}(\boldsymbol{\nu}_R)\boldsymbol{\nu}_R = \boldsymbol{\tau} \tag{2}$$

where $\boldsymbol{\tau} = [X, Y, N]^T \in \mathbb{R}^3$ is the vector expressing the longitudinal and lateral forces and moment, $\mathbf{M}$ is the inertia matrix, $\mathbf{C_{RB}}$ is the Coriolis matrix, $\mathbf{C_A}$ is the hydrodynamics Coriolis and centripetal matrix, $\mathbf{D}$ is the damping matrix, $\boldsymbol{\nu} = [u, v, r]^T \in \mathbb{R}^3$ is the vessel generalised velocity vector in the body-fixed frame $\underline{b}$, $\boldsymbol{\nu_R} = [u_R, v_R, r]^T \in \mathbb{R}^3$ is the relative speed between the ship and the current, $\dot{\boldsymbol{\nu}} = [\dot{u}, \dot{v}, \dot{r}]^T \in \mathbb{R}^3$ is the ship acceleration in the $\underline{b}$ frame, $\dot{\boldsymbol{\eta}} = [\dot{x}, \dot{y}, \dot{\psi}]^T \in \mathbb{R}^3$ is the generalised velocity vector in the inertial frame $\underline{n}$, $\mathbf{R}(\psi)$ is the rotation matrix, and $\psi \in \mathbb{R}$ is the heading angle.

The inertia matrix $\mathbf{M}$ is defined as $\mathbf{M} = \mathbf{M}_{RB} + \mathbf{M}_A$ (3), namely, it is the sum of the rigid body inertia matrix $\mathbf{M}_{RB}$ and the added mass matrix $\mathbf{M}_A$. The Coriolis matrices are the rigid body Coriolis matrix $\mathbf{C}_{RB}$ (4) and the hydrodynamics Coriolis and centripetal matrix $\mathbf{C}_A$ (5). Finally, the damping matrix $\mathbf{D}$ is defined as $\mathbf{D} = \mathbf{D}_L + \mathbf{D}_{NL}$ (6), therefore, as the sum of the linear viscous damping $\mathbf{D}_L$ and of the nonlinear damping $\mathbf{D}_{NL}(\boldsymbol{\nu}_R)$, see [17].

$$\mathbf{M} = \begin{bmatrix} m - X_{\dot{u}} & 0 & 0 \\ 0 & m - Y_{\dot{v}} & -Y_{\dot{r}} \\ 0 & -Y_{\dot{r}} & I_Z - N_{\dot{r}} \end{bmatrix} \tag{3}$$

$$\mathbf{C}_{RB}(\boldsymbol{\nu}) = \begin{bmatrix} 0 & 0 & -mv \\ 0 & 0 & mu \\ mv & -mu & 0 \end{bmatrix} \tag{4}$$

$$\mathbf{C}_A(\boldsymbol{\nu}_R) = \begin{bmatrix} 0 & 0 & Y_{\dot{v}} v_R + Y_{\dot{r}} r \\ 0 & 0 & -X_{\dot{u}} u_R \\ -Y_{\dot{v}} v_R - Y_{\dot{r}} r & X_{\dot{u}} u_R & 0 \end{bmatrix} \tag{5}$$

$$\mathbf{D}(\boldsymbol{\nu}_R) = \begin{bmatrix} d_{11}(\boldsymbol{\nu}) & 0 & 0 \\ 0 & d_{22}(\boldsymbol{\nu}) & d_{23}(\boldsymbol{\nu}) \\ 0 & d_{32}(\boldsymbol{\nu}) & d_{33}(\boldsymbol{\nu}) \end{bmatrix} \tag{6}$$

where $d_{11}(\boldsymbol{\nu}) = -X_u - X_{|u|u}|u_R| - X_{uuu}u_R$, $d_{22}(\boldsymbol{\nu}) = -Y_v - Y_{|v|v}|v_R| - Y_{v|r|}|r| - Y_{vvv}v_R$, $d_{23}(\boldsymbol{\nu}) = -Y_r - Y_{|v|r}|v_R| - Y_{|r|r}|r|$, $d_{32}(\boldsymbol{\nu}) = -N_v - N_{|v|v}|v_R| - N_{v|r|}|r|$, $d_{33}(\boldsymbol{\nu}) = -N_r - N_{|v|r}|v_R| - N_{|r|r}|r| - N_{rrr}r$, $m \in \mathbb{R}^+$ is the mass of the vessel, $I_Z \in \mathbb{R}^+$ is the vessel inertia, the other elements of matrix $\mathbf{M}$ are the added mass coefficients, and the used symbols for the hydrodynamic coefficients follow the stadard SNAME [18] convention; see also [16] for further details.

The control input vector $\tau \in \mathbb{R}^3$ is given by the action of the four azimuth thrusters placed at the four corners of the vessel, as shown in Figure 1. Each thruster can be used within a 90° angle sector, where the working ranges are defined by an interval of ±45° from the reference angle $\alpha_i^* \in \mathbb{R}^3$. Two options are identified for choosing the α_i^* angle: The first is to select the reference angle along the bisectors of the vessel reference frame $\underline{b}$, this configuration is named α_A^* and is shown in the portside part of Figure 1; the second is to choose the reference angle along the diagonals of the rectangular defined by the four actuators, this configuration is named α_B^* and is shown in the starboard part of Figure 1.

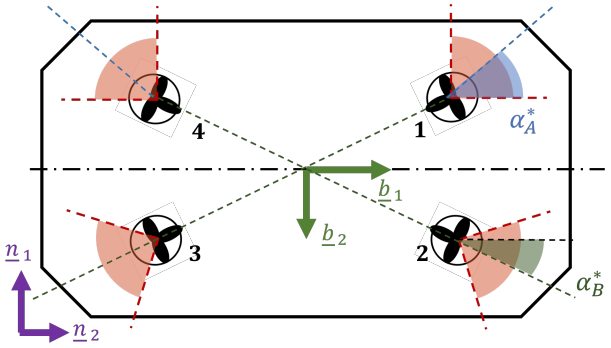

Fig. 1: Azimuthal operational ranges.

The dynamics of each thruster is expressed through the dynamics of the azimuth angle and the propulsion system. In the first case, the sigmoid function in (7) proposed in [19] is adopted, while, in the second case, the first order function in (8) is used in order to describe motor dynamics and, as a consequence, to set the dynamic thrust.

$$\dot{\alpha} = K_\alpha \frac{\alpha_d - \alpha}{\sqrt{(\alpha_d - \alpha)^2 + \varepsilon^2}} \tag{7}$$

$$\dot{\omega} = K_\omega(\omega_d - \omega) \tag{8}$$

where $\alpha_d \in \mathbb{R}$ is the desired azimuth angle, $K_\alpha \in \mathbb{R}^+$ is a constant representing the rotational velocity, $\varepsilon \in \mathbb{R}^+$ is a tuning parameter to adjust the transient behaviour, $K_\omega \in \mathbb{R}^+$ is a constant representing the total inertia (the inertia of the shaft, electric motor and propeller and its added mass), $\omega_d \in \mathbb{R}$ is the desired motor speed, and $\omega \in \mathbb{R}$ is the motor speed. Finally, the vector $\tau_i \in \mathbb{R}^3$ of each propulsor is computed by rotating the thrust from the propulsor to the $\underline{b}$ frame as in (9).

$$\boldsymbol{\tau}_{AZ_i} = \begin{bmatrix} cos(\alpha_i) \\ sin(\alpha_i) \\ x_{AZ_i} sin(\alpha_i) - y_{AZ_i} cos(\alpha_i) \end{bmatrix} T_i \tag{9}$$

where (x_{AZ_i}, y_{AZ_i}) are the coordinates of the i^{th} thruster in the $\underline{b}$ frame.

III. CONTROLLER PIPELINE

The controller pipeline is shown in Figure 2, and in this paper, different solutions for each controller subsystem are explored, and different combinations are tested with the common pipeline for the entire speed range of the vessel. The pipeline starts with the computation of the desired time trajectory by the reference model starting from the desired waypoint list given as input; after the error between the desired and the feedback state value is evaluated and the proper thrust loads and moment needed to move as desired are computed by the motion controller; finally, the allocation system allocates the control signals to the actuators. The allocation module can be divided into two parts: The Force Allocation Logic (FAL), which computes the required thrust

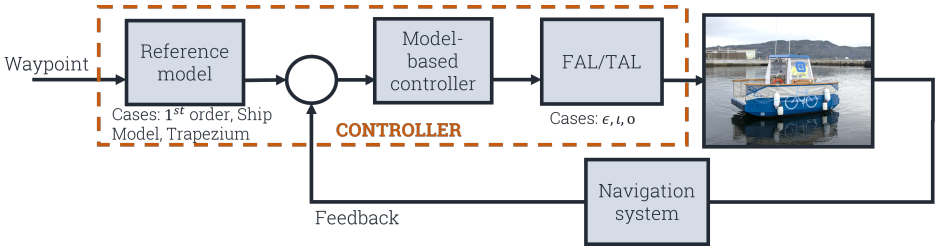

Fig. 2: Model-based controller pipeline for the milliAmpere1 prototype ferry.

for each actuator, and the Thrust Allocation Logic (TAL), which computes the right setpoints for each actuator. In this application, azimuth angle and motor speed setpoints are needed. The first will be an output of the FAL, and the second one is computed thanks to a combinator curve starting from the desired thrust. The setpoints are sent to the vessel, and the navigation system computes the feedback values.

The proposed solution is designed to be able to cover the entire speed range of the ferry. Two different controllers with the same layout are outlined and can operate in two different speed ranges that have been distinctly defined and will hence be referred to as low- and higher-speed. These definitions are related to the speed range in which the ferry can operate.

IV. MODEL-BASED CONTROLLER

The controller is chosen to be a model-based PID stated in (10) for all the speed ranges. The control action $\boldsymbol{\tau}_C \in \mathbb{R}^3$ is the sum of two contributions: A model-based feedforward term $\boldsymbol{\tau}_{FF} \in \mathbb{R}^3$ and a feedback term $\boldsymbol{\tau}_{FB} \in \mathbb{R}^3$.

$$\boldsymbol{\tau}_C = \boldsymbol{\tau}_{FF} + \boldsymbol{\tau}_{FB} \tag{10}$$

The feedforward term is computed through the vessel model calculated on desired setpoints as shown in (11). This term will compute the necessary loads to obtain the desired changes in the setpoint, leaving the feedback controller to deal with model uncertainties and environmental disturbances.

$$\boldsymbol{\tau}_{FF} = \mathbf{M}\dot{\boldsymbol{\nu}}_{TR} + \mathbf{D}(\boldsymbol{\nu}_{TR})\boldsymbol{\nu}_{TR} + \mathbf{C}(\boldsymbol{\nu}_{TR})\boldsymbol{\nu}_{TR} \tag{11}$$

where $\boldsymbol{\eta}_{TR} \in \mathbb{R}^3$ is the desired pose trajectory in the $\underline{n}$ frame and $\boldsymbol{\nu}_{TR} \in \mathbb{R}^3$ is the desired velocity in the $\underline{b}$ frame.

The feedback term is chosen as the Proportional Integrative and Derivative (PID) controller stated in (12) for the low-speed controller, and using only the Proportional and Derivative (PD) controller for higher-speed operation by setting the integral gain equal to zero since the setpoints are continuously changing. The PID terms are functions of the pose error $\mathbf{e} \in \mathbb{R}^3$ (13) and the velocity error $\boldsymbol{\nu}_e \in \mathbb{R}^3$ (14).

$$\boldsymbol{\tau}_{FB} = \mathbf{K}_P\mathbf{e} + \mathbf{K}_I \int_0^t \mathbf{e}(\tau)d\tau + \mathbf{K}_D\boldsymbol{\nu}_e \tag{12}$$

$$\mathbf{e} = \mathbf{R}^T(\psi)(\boldsymbol{\eta}_{TR} - \boldsymbol{\eta}) \tag{13}$$

$$\boldsymbol{\nu}_e = \boldsymbol{\nu}_{TR} - \boldsymbol{\nu} \tag{14}$$

where $\mathbf{K}_P$, $\mathbf{K}_I$, and $\mathbf{K}_D$ are positive diagonal matrices containing the proportional, integral, and derivative gains, respectively.

V. FORCE ALLOCATION LOGIC

Each thruster can be controllable with two inputs: The motor speed and the azimuth angle. Four thrusters are installed onboard, so eight control inputs are needed, resulting in an over-actuated system with infinite solutions to the force allocation problem. To solve the problem, several techniques are proposed in the literature as reported in [7] and [8]. This work proposes three solutions for the low-speed range: two optimal allocations solved in real time and a semi-optimal analytical solution. For the higher-speed range, only the semi-optimal one is considered because keeping the angles fixed is beneficial for the ferry's course stability, as even small variations in azimuth angle at higher speed lead to significant variations in the heading.

A. Real-time optimal force allocation

The allocation problem is formulated as the constrained optimisation problem of (15) where the aim is to minimise an objective function $f(\mathbf{x})$ in the variables $\mathbf{x}$ under the equality $h(\mathbf{x})$ and inequality constraints $g(\mathbf{x})$ with the lower bounds $\mathbf{lb}$ and upper bounds $\mathbf{ub}$. Two different optimisation problems are identified by defining two objective functions and two inequality constraints. The problem is solved numerically through the nonlinear programming solver by Matlab.

$$\begin{aligned} \underset{\mathbf{x}}{\text{minimize}} \quad & f(\mathbf{x}) \\ \text{subject to} \quad & h(\mathbf{x}) = \mathbf{0}, \\ & \mathbf{x}(0) = \mathbf{x}_0, \\ & \mathbf{lb} \leq \mathbf{x} \leq \mathbf{ub}, \\ & g(\mathbf{x}) \leq \mathbf{0} \end{aligned} \tag{15}$$

The unknowns of the problem are the thruster load, the direction, and the corresponding rectangular force components defined for each thruster: $\mathbf{x} = [X_i, Y_i, T_i, \alpha_i]^T$, $i = 1, ..., 4$.

The equality constraints are given by the static equilibrium in the horizontal plane and by the relationships between the unknowns, as given by (16).

$$h(\mathbf{x}) = \begin{cases} \sum_{i=1}^4 X_i - \tau_C(1) \\ \sum_{i=1}^4 Y_i - \tau_C(2) \\ \sum_{i=1}^4 (x_{az_i}, y_{az_i}) \times (X_i, Y_i) - \tau_C(3) \\ T_i^2 - X_i^2 - Y_i^2 \\ \alpha_i - atan2(Y_i, X_i) \end{cases} \tag{16}$$

The bounds **lb** and **ub** set the limits on the azimuth angles α_i (as mentioned in Section II each actuator can operate in a range of $\pm 45°$) and on the magnitude of the thrust T_i.

A set of inequality constraints $g(\mathbf{x})$ is defined to put a limit on the derivative of the azimuth angles $\dot{\alpha}_i \in \mathbb{R}$ to limit their movements according to:

$$g(\mathbf{x}) = \dot{\alpha}_i - \dot{\alpha}_{max_i} \leq 0 \; i = 1,..,4 \tag{17}$$

where $\dot{\alpha}_{max_i}$ is the maximum value of the derivative given by the actuator limits.

The adopted objective function tends to minimise the total thrust of the actuators, taking into account a penalty in the changes of the angle α and of the thrust T as:

$$\begin{aligned} f(\mathbf{x}) = \sum_{i=1}^{4} \mathbf{t}_i^T \mathbf{W}_i \mathbf{t}_i + (\alpha - \alpha_{t-1})' \mathbf{\Omega} \\ (\alpha - \alpha_{t-1}) + (\mathbf{T} - \mathbf{T}_{t-1})' \mathbf{Q} (\mathbf{T} - \mathbf{T}_{t-1}) \end{aligned} \tag{18}$$

where $\mathbf{t}_i = [X_i, Y_i]$, $\alpha_{t-1} \in \mathbb{R}^4$ is the vector of the actuator angles at the previous time step, $\mathbf{T}_{t-1} \in \mathbb{R}^4$ is the vector of thrust magnitudes at the previous time step, $\mathbf{W}_i \in \mathbb{R}^{4x4}$ is a weight diagonal matrix penalising the square of the maximum allowable thrust $T_{max_i} \in \mathbb{R}$ of each actuator, $\mathbf{\Omega} \in \mathbb{R}^{4x4}$ is a diagonal matrix penalising the square of the maximum $\Delta\alpha$ considered, and $\mathbf{Q} \in \mathbb{R}^{4x4}$ is a diagonal matrix penalising the maximum thrust. The values chosen for W_i, Ω, and Q affect the performance of the thrust allocation in how the thrusters are used to generate the commanded τ_C. The chosen values are kept constant in all the pipelines.

B. Semi-optimal allocation

The allocation problem is also solved using the Lagrange Multipliers method [10] to obtain an analytical solution. The actuator angles are kept fixed and selected between two different configurations according to the main direction of the required control force for the low-speed range and with one configuration for the higher-speed range. Hence, the problem can be defined as a semi-optimal one and the unknowns of the problem $\mathbf{x}$ are $[T_1, T_2, T_3, T_4]^T$. The problem that is going to be solved through the Lagrange method is stated in (19) where: The objective function $f(\mathbf{x})$ is the one previously defined in (18) with $\mathbf{Q} = \mathbf{\Omega} = \mathbf{0}$; the equality constraints $h(\mathbf{x})$ are given by the equilibrium in the horizontal place (see the first three lines of (16)); and the lower and the upper bounds (**lb** and **ub**) wants to set the limit on the minimum and the maximum value of the thrust load.

$$\begin{aligned} \underset{\mathbf{x}}{\text{minimize}} \quad & f(\mathbf{x}) \\ \text{subject to} \quad & h(\mathbf{x}) = 0, \\ & \mathbf{x}(0) = \mathbf{x}_0, \\ & \mathbf{lb} \leq \mathbf{x} \leq \mathbf{ub} \end{aligned} \tag{19}$$

Hence, an analytical solution for $[T_1, T_2, T_3, T_4]^T$ is found as function of the control force τ_C and the azimuth angles α.

The selected azimuth angle quadruplets selected are:

- Low-speed with configuration α_B^*: $[0°, 0°, 135° - \alpha_B^*, 270° - \alpha_B^*]$ & $[-\alpha_B^*, 90° - \alpha_B^*, 180° + \alpha_B^*, 270° - \alpha_B^*]$;
- Low-speed with configuration α_A^*: $[0°, 0°, 90°, 270°]$ & $[0°, 90°, 90°, 180°]$;
- Higher-speed: $[5°, -5°, 225° - \alpha_B^*, 135° + \alpha_B^*]$.

VI. REFERENCE MODELS

The desired waypoints are sent to a reference model to compute a smooth, time-varying reference trajectory. This paper utilises three reference models for the low-speed controller and one for the higher-speed controller.

Several options can be used to fulfil this aim, but this paper considers three options for the low-speed range and one for the higher-speed range. In all cases, the input is the final desired waypoint position $\boldsymbol{\eta}_d \in \mathbb{R}^3$, while the outputs are the trajectory in terms of pose $\boldsymbol{\eta}_{TR}$ in the $\underline{n}$ frame and of velocity $\boldsymbol{\nu}_{TR}$ in the $\underline{b}$ frame.

A. Low-speed reference model

The first reference model adopted is the first-order lowpass filter in (20). It is the simplest form for a reference model and, if properly tailored, can compute a feasible trajectory.

$$\dot{\boldsymbol{\eta}}_{TR} = \frac{1}{\tau_1} (\boldsymbol{\eta}_{TR} - \boldsymbol{\eta}_d) \tag{20}$$

where $\tau_1 \in \mathbb{R}^+$ is a constant.

The second reference model is the physically-based vessel model shown in (21).

$$\mathbf{M}\dot{\boldsymbol{\nu}}_{tr} + (\mathbf{D} + \mathbf{C})\boldsymbol{\nu}_{TR} = -(\mathbf{K}_P \mathbf{e}^* + \mathbf{K}_I \int_0^t \mathbf{e}^* d\tau + \mathbf{K}_D \boldsymbol{\nu}_{TR}) \tag{21}$$

where $\mathbf{e}^* = \mathbf{R}^T(\psi)(\boldsymbol{\eta}_{TR} - \boldsymbol{\eta}_d)$ is the error between the computed trajectory and the selected waypoint.

The third reference model is a trapezoidal speed law between the two selected waypoints. The speed law is similar to the one in Figure 4 where $V_{max} \in \mathbb{R}^+$ is the selected maximum speed, $V_{min} \in \mathbb{R}^+$ is selected equal to zero, and $t_{end} \in \mathbb{R}^+$ is the time in which it is supposed to cover the segment between the selected waypoints. The pose trajectory is computed according to the defined speed law. The approach is comparable to the one described below for the higher-speed phase.

B. Higher-speed reference model

The reference model adopted for the higher-speed is again a trapezium speed law between the selected waypoints. Indeed, at each time step, two waypoints are selected (WP_1 and WP_2) from the waypoint list given as input, and the $\underline{f}$ reference frame can be defined, see Figure 3. It has the origin on WP_1 and points to WP_2, outlining the angle $\gamma \in \mathbb{R}$ between the positive unit vector $\underline{n}_1$ of the inertial reference frame and $\underline{f}_1$. The switch at the following waypoints couple occurs when the alongtrack distance to WP_2, $d_{sw} = (WP_2 - \eta)\underline{f}_1 \in \mathbb{R}$, is lower than nL_{PP}.

The speed law is defined according to the trapezium speed law in Figure 4. As it is possible to see from the figure,

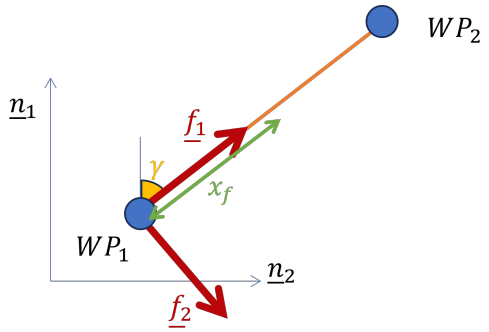

Fig. 3: Higher-speed reference frame.

the speed law is composed of four phases: the first phase starts at t_0 when switching to the next waypoint and has an acceleration from the chosen minimum speed $V_{min} \in \mathbb{R}^+$ to the chosen maximum value $V_{max} \in \mathbb{R}^+$, and ending at t_1; the second phase keeps V_{max} constant up to time t_2; the third phase has a deceleration up to time t_3 when it reaches V_{min}; and the fourth phase when it reaches WP_2 with the minimum speed. The time steps are defined as:

$$\begin{aligned} t_1 &= t_0 + \frac{2d^*}{V_{max}+V_{min}} \\ t_2 &= t_1 + \frac{d_{WP} - 2d^* - nL_{pp}}{V_{max}} \\ t_3 &= t_2 + \frac{2d^*}{V_{max}+V_{min}} \end{aligned} \tag{22}$$

where d_{WP} is the distance between the selected waypoints and $d^* \in \mathbb{R}^+$ is the distance for which the acceleration phase is designed.

The desired position x_f along $\underline{f}_1$ is defined by the kinematics outlined by the speed and then rotated to the $\underline{n}$ frame to have the desired position trajectory. The desired heading angle is γ, which is the angle between the two active waypoints.

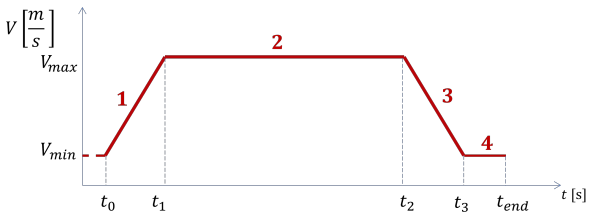

Fig. 4: Trapezium speed law.

VII. PERFORMANCE METRICS

The low-speed controllers are evaluated through five performance metrics. Several methods for comparing the controller performance can be defined, but the well-known performance metrics defined in [20] are adopted here.

The Integral of Absolute Error ($IAE \in \mathbb{R}$) was introduced in [21] as a measure of the system error, and it is defined as in (23) with the error of (24). Its variation is also added for an initial evaluation of the different reference models for the low-speed range, which is called $IAE - RF \in \mathbb{R}$ and is formulated as in (25), which is a function of the error $e_{IAE-RF} \in \mathbb{R}$ between the trajectories computed by each reference filter and the four corner square. To take into account also the energy consumption, the absolute value of the error multiplied by the energy consumption ($IAEW \in \mathbb{R}$) is proposed in [22], and is defined as in (26) with the power consumption of (27). This penalises the error linearly with the magnitude and is a measure of control precision. To take into account the actuator wear and tear and to penalise actuator changes, the Integral of Absolute Differentiated Control ($IADC \in \mathbb{R}$) is suggested in [23] and is defined as in (28) with the normalised thrust vector of (29). To take into account the actuation error, the Integral of Absolute Thrust Error ($IATE \in \mathbb{R}$) is defined as in (30) with the error in (31).

$$IAE = \int_0^t e_{IAE}(\varepsilon)d\varepsilon \tag{23}$$

$$e_{IAE} = \sqrt{\boldsymbol{e}^T \boldsymbol{W}_{IAE} \boldsymbol{e}} \tag{24}$$

$$IAE - RF = \int_0^t e_{IAE-RF}(\varepsilon)d\varepsilon \tag{25}$$

$$IAEW = \int_0^t e_{IAE}(\varepsilon)d\varepsilon \int_0^t P(\varepsilon)d\varepsilon \tag{26}$$

$$P(t) = |\boldsymbol{v}^T \boldsymbol{W}_\tau \boldsymbol{\tau}_C| \tag{27}$$

$$IADC = \int_0^t \dot{\tau}^*(\varepsilon)d\varepsilon \tag{28}$$

$$\dot{\tau}^* = \sqrt{\dot{\boldsymbol{\tau}}_C^T \boldsymbol{W}_\tau \dot{\boldsymbol{\tau}}_C} \tag{29}$$

$$IATE = \int_0^t e_{IATE}(\varepsilon)d\varepsilon \tag{30}$$

$$e_{IATE} = \sqrt{(\boldsymbol{T} - \boldsymbol{T}_{act})^T \boldsymbol{W}_{IATE} (\boldsymbol{T} - \boldsymbol{T}_{act})} \tag{31}$$

where $\boldsymbol{W}_{IAE}$ is a diagonal matrix penalising the pose error, $\boldsymbol{W}_\tau$ is a diagonal matrix penalising the time-differentiated thrust vector, $\boldsymbol{T}_{act} \in \mathbb{R}^4$ is the actuated thrust, and $\boldsymbol{W}_{IATE}$ is a diagonal matrix penalising the thrust error.

VIII. SIMULATION RESULTS

The proposed controllers for the low-speed range are tested through simulations with a four-corner test scenario as reported in [24]. The four-corner test allows the evaluation of the trajectory tracking capabilities of the ferry for each degree of freedom and with the coupled motions. During the test, the following waypoints are reached: The starting point is the pose $[0,\ 0,\ 0°]^T$, then the ferry moves to $[l,\ 0,\ 0°]^T$ with a pure surge motion, then it moves in $[l,\ l,\ 0°]^T$ with a pure sway motion, then it rotates up to $[l,\ l,\ 45°]^T$ with a pure rotation motion, then it moves in $[0,\ l,\ 45°]^T$ coupling the surge and sway movements, and finally it comes back to $[0,\ 0,\ 0°]^T$, thus coupling all the motions. In this work, the side of the square l is assumed to be equal to $10m$ in these tests and the time assumed to cover one side is assumed to be $100s$.

Reference Model	IAE – RF
1^{st} order	2.48
Vessel model	12.48
Trapezium	0

TABLE I: IAE-RF.

The first evaluation is done on the proposed reference models of Section VI on the four-corner trajectory with the IAE-RF metrics. The results in terms of $IAE - RF$ are reported in Table I. From these, it is possible to see that the trapezium and the 1^{st} order model have small values of $IAE - RF$, while the vessel model has the biggest value due to some delays that arise when there is a change in the corner. Hence, only the trapezium and the 1^{st} order reference model are considered in the following.

In the above sections, different proposals have been made for the reference angle α_i^* (see Section II), the reference model (RM) (see Section VI), and the force allocation logic (FAL) (see Section V), hence results from different tests are proposed and summarised in the first four columns of Table II. The acronyms adopted in the column FAL have the following meaning: $\boldsymbol{\varepsilon}$, real-time optimal allocation of Section V-A with no inequality constraints and the objective function of (18) with $\mathbf{Q} = \boldsymbol{\Omega} = \mathbf{0}$; $\boldsymbol{\iota}$, real-time optimal allocation of Section V-A with the inequality constraints of (17) and the objective function of (18); and $\mathbf{o}$, semi-optimal allocation of Section V-B.

The results, in terms of the KPI highlighted in Section VII are shown in the last three columns of Table II and in figures 5, 6, 7, and 8. The table values correspond to the metrics values at the last simulation time step, i.e. at the end of the four-corner test, while the total time histories are reported in the figures. All simulations have the same total and partial time extension to make them comparable. Lower metrics mean better performance in terms of precision, energy consumption, actuator wear and tear, and actuation error. As it is possible to see from the results, in general, the cases with the 1^{st} order reference model have better values of IAE and $IAEW$, which means higher precision, while the cases with the allocation ι and o have, as expected, the smallest values of $IADC$, which means they move the actuators less. Allocation ε is generally the best in terms of $IATE$. The best value of each metric is highlighted in bold in Table II.

Finally, the results concerning cases 3, 7, 8, and 10 are reported in terms of trajectory and pose errors in the $\underline{n}$ frame in figures 9 and 10, respectively. In all the figures, in blue are marked the time histories related to test case 3, with the green dashed line the data related to test case 7, with the red dash-dotted line the data related to test case 8, and with the dotted light blue line the data related to test case 10. From the trajectories time histories, it is possible to see the difference between the two reference models that leads to the different values of the $IAE - RF$ values of Table I; while from the others, it is possible to see that errors are born when the corners are switched (every 100 s). Since this

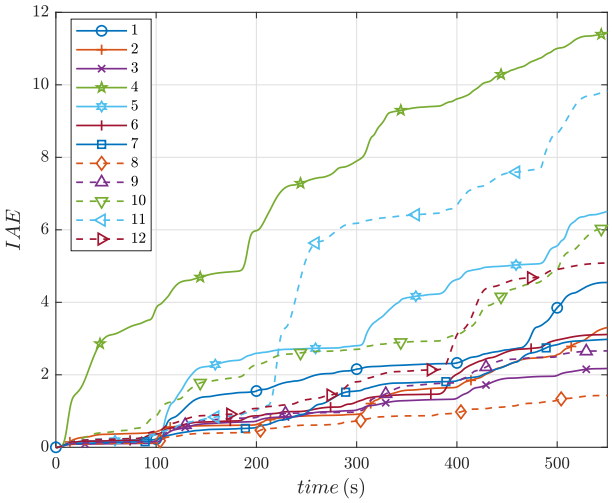

Fig. 5: Low-speed configurations tests: IAE.

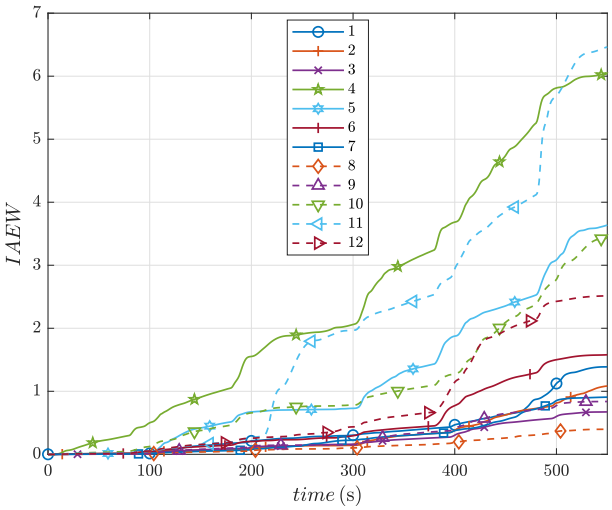

Fig. 6: Low-speed configurations tests: IAEW.

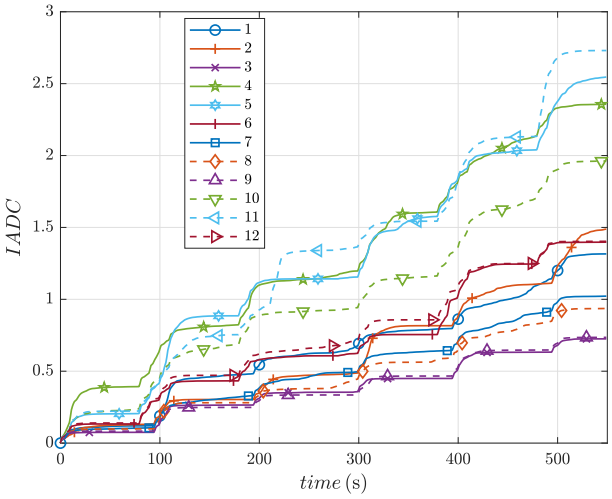

Fig. 7: Low-speed configurations tests: IADC.

Case	α_i^*	RM	FAL	IAE	IAEW	IADC	IATE
1	α_A^*	1^{st} order	ε	4,55	1,39	1,32	6,23
2	α_A^*	1^{st} order	ι	3,30	1,08	1,49	11,88
3	α_A^*	1^{st} order	o	2,17	0,67	**0,72**	7,36
4	α_A^*	Trapez.	ε	11,42	6,04	2,36	9,03
5	α_A^*	Trapez.	ι	6,51	3,64	2,55	15,78
6	α_A^*	Trapez.	o	3,11	1,58	1,40	14,21
7	α_B^*	1^{st} order	ε	2,98	0,91	1,02	**3,91**
8	α_B^*	1^{st} order	ι	**1,43**	**0,40**	0,94	5,11
9	α_B^*	1^{st} order	o	2,66	0,84	0,74	8,5
10	α_B^*	Trapez.	ε	6,04	3,43	1,96	5,77
11	α_B^*	Trapez.	ι	9,84	6,46	2,73	16,65
12	α_B^*	Trapez.	o	5,09	2,51	1,40	11,12

TABLE II: Tests of low-speed controller configurations.

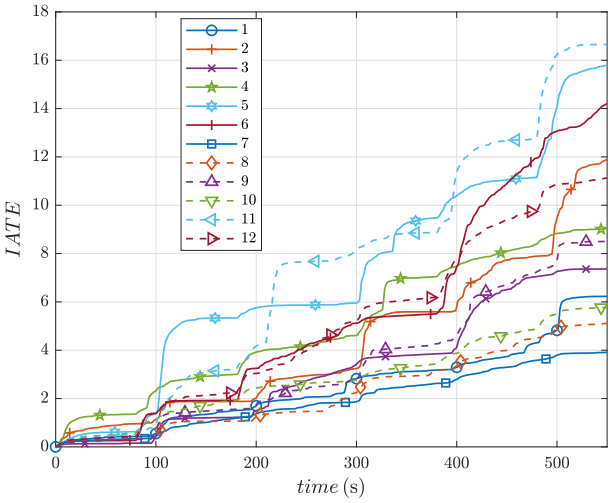

Fig. 8: Low-speed configurations tests: IATE.

application aims to have high precision and reduced azimuth movements, case 8 can be considered a good trade-off for this case, together with the reference angle α_B^* selection.

The proposed higher-speed controller is tested with a series of waypoints that lead to several heading changes. The desired path is highlighted in blue in Figure 11 and defined according to the waypoint list of Table III. Here, in the first column, there is the waypoint number; in the second and third columns, the position of the waypoints in the $\underline{n}$ frame is defined; while in the last two columns, the angle γ (in degrees) and the distances between each couple of waypoints, made of the one in the same line and the one in the line before, are computed.

n	x_{WP}	y_{WP}	γ	d_{wp}
1	0	0		
2	$20L_{PP}$	$50L_{PP}$	69	$53L_{PP}$
3	$30L_{PP}$	$100L_{PP}$	79	$51L_{PP}$
4	$15L_{PP}$	$150L_{PP}$	106	$52L_{PP}$
5	$15L_{PP}$	$200L_{PP}$	90	$50L_{PP}$
5	$80L_{PP}$	$300L_{PP}$	56	$120L_{PP}$

TABLE III: Higher-speed Scenario.

The result, in terms of the resultant trajectory, is highlighted with the red line in Figure 11. The pose errors time plots in the $\underline{f}$ reference frame are reported in Figure 12. As it is possible to see from the results, errors in terms of speed

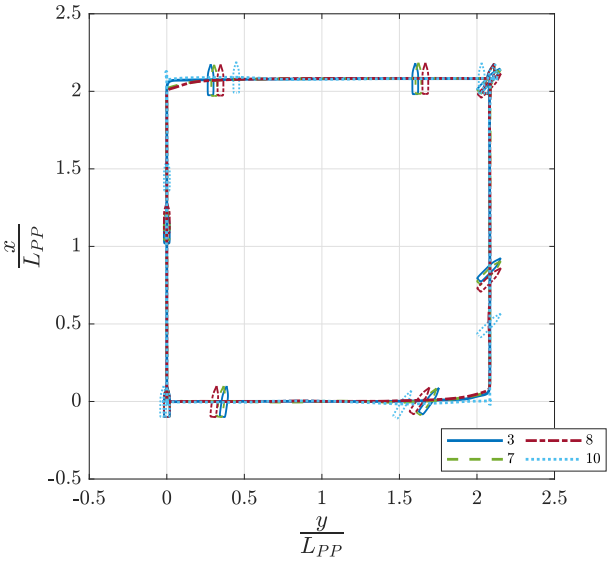

Fig. 9: Low-speed configurations: Trajectories.

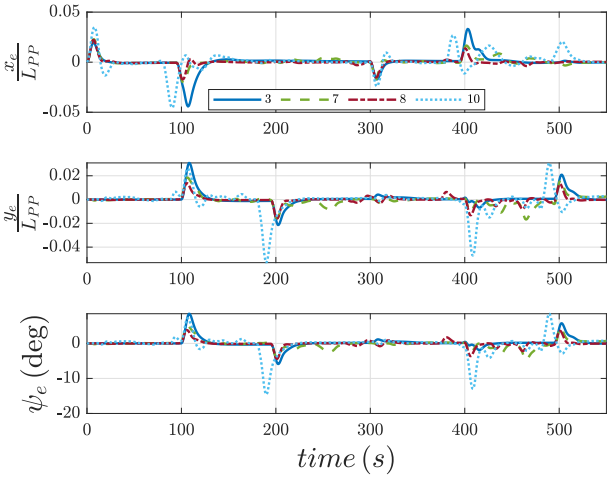

Fig. 10: Low-speed configurations: Pose errors $\underline{n}$ frame.

and pose arise, as expected, after each switch, while the long error $\underline{f}_1$ converges on the selected value for the switch nL_{PP}.

IX. CONCLUSIONS

This paper presents the initial stage of the development of a model-based controller for the milliAmpere1 passenger ferry prototype following its propulsion plant upgrade. Two separate controllers for the low- and the higher-speed ranges are defined with the same controller pipeline and evaluated through numerical simulation. In particular, a comparison between different reference models, force allocation algorithms, and reference angles α_i^* for the low-speed range, is carried out by using some selected performance metrics, and their behaviours are presented. Starting from these results, a solution for the higher-speed range is found for fulfilling the tracking objective. In future work, experimental tests of the proposed pipelines are planned to validate the simulated results and investigate the transition phase between the two

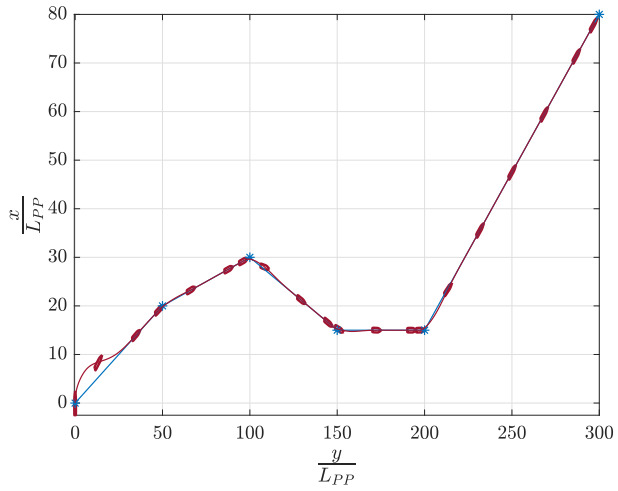

Fig. 11: Higher-speed configuration: Trajectory.

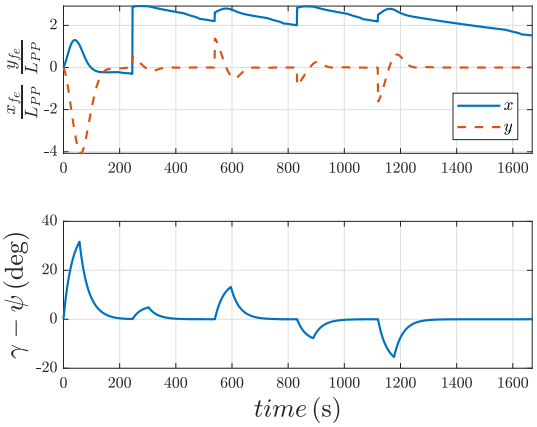

Fig. 12: Higher-speed configuration: Pose errors f frame.

motion controllers. This involves implementing the proposed control system and carrying out experimental tests. The resulting responses of the proposed motion control system and algorithms will then be compared and discussed with respect to the responses of a baseline control system.

References

[1] T. P. Hughes, *Elmer Sperry: Inventor and engineer*. Johns Hopkins University Press, 1971.

[2] N. Minorsky, "Directional stability of automatically steered bodies," *Journal of the American Society for Naval Engineers*, vol. 34, no. 2, pp. 280–309, 1922.

[3] T. I. Fossen, "A survey on nonlinear ship control: From theory to practice," *IFAC Proceedings Volumes*, vol. 33, no. 21, pp. 1–16, 5th IFAC Conference on Manoeuvring and Control of Marine Craft (MCMC 2000), Aalborg, Denmark, 23-25 August 2000.

[4] S. Donnarumma, M. Figari, M. Martelli, S. Vignolo, and M. Viviani, "Design and validation of dynamic positioning for marine systems: A case study," *IEEE Journal of Oceanic Engineering*, vol. 43, no. 3, pp. 677–688, 2018.

[5] A. B. Martinsen, A. M. Lekkas, and S. Gros, "Reinforcement learning-based NMPC for tracking control of ASVs: Theory and experiments," *Control Engineering Practice*, vol. 120, p. 105024, 2022.

[6] A. J. Sørensen, "A survey of dynamic positioning control systems," *Annual Reviews in Control*, vol. 35, no. 1, pp. 123–136, 2011.

[7] C. De Wit, "Optimal thrust allocation methods for dynamic positioning of ships," Master's thesis, TU Delft, 2009.

[8] T. A. Johansen and T. I. Fossen, "Control allocation—a survey," *Automatica*, vol. 49, no. 5, pp. 1087–1103, 2013.

[9] E. H. Thyri, G. Bitar, and M. Breivik, "A 3 DOF path-following controller for a non-directionally stable vessel with slow thruster dynamics," *IFAC-PapersOnLine*, vol. 54, no. 16, pp. 288–294, 13th IFAC Conference on Control Applications in Marine Systems, Robotics, and Vehicles CAMS 2021.

[10] M. Martelli, N. Faggioni, and S. Donnarumma, "A time-domain methodology to assess the dynamic positioning performances," *Ocean Engineering*, vol. 247, p. 110668, 2022.

[11] S. Donnarumma, M. Figari, M. Martelli, and R. Zaccone, "Simulation of the guidance and control systems for underactuated vessels," in *Modelling and Simulation for Autonomous Systems*, J. Mazal, A. Fagiolini, and P. Vasik, Eds. Cham: Springer International Publishing, 2020, pp. 108–119.

[12] DNV, "The ReVolt. a new inspirational ship concept." [Online]. Available: https://www.dnv.com/maritime/autonomous-remotely-operated-ships/research-activities.html

[13] A. Skredderberget, "The first ever zero emission, autonomous ship," "https://www.yara.com/knowledge-grows/game-changer-for-the-environment/", 2018.

[14] Zeabuz, "Launching the world's first commercial, emission-free, autonomous passenger ferry in the heart of the city," "https://www.zeabuz.com/torghatten-and-zeabuz-make-history-in-stockholm/", 2023.

[15] E. F. Brekke, E. Eide, B.-O. H. Eriksen, E. F. Wilthil, M. Breivik, E. Skjellaug, Ø. K. Helgesen, A. M. Lekkas, A. B. Martinsen, E. H. Thyri *et al.*, "milliAmpere: An autonomous ferry prototype," in *Journal of Physics: Conference Series*, vol. 2311, no. 1. IOP Publishing, 2022, pp. 12–29.

[16] T. I. Fossen, *Handbook of marine craft hydrodynamics and motion control*. John Wiley & Sons, 2011.

[17] M. Martelli, *Marine propulsion simulation: Methods and Results*. Walter de Gruyter GmbH & Co KG, 2015.

[18] SNAME, "Nomenclature for treating the motion of a submerged body through a fluid," *The Society of Naval Architects and Marine Engineers, Technical and Research Bulletin*, no. 1950, pp. 1–5, 1950.

[19] A. A. Pedersen, "Optimization based system identification for the milliampere ferry," Master's thesis, Norwegian University of Science and Technology (NTNU), Trondheim, Norway, 2019.

[20] M. E. N. Sørensen, "Topics in nonlinear and model-based control of ships," Ph.D. dissertation, Norwegian University of Science and Technology (NTNU), Trondheim, Norway, 2021.

[21] F. C. Fickeisen and T. M. Stout, "Analogue methods for optimum servomechanism design," *Transactions of the American Institute of Electrical Engineers, Part II: Applications and Industry*, vol. 71, no. 5, pp. 244–250, 1952.

[22] M. E. N. Sørensen and M. Breivik, "Comparing nonlinear adaptive motion controllers for marine surface vessels," *IFAC-PapersOnLine*, vol. 48, no. 16, pp. 291–298, 2015, 10th IFAC Conference on Manoeuvring and Control of Marine Craft MCMC 2015.

[23] B.-O. H. Eriksen and M. Breivik, "Modeling, identification and control of high-speed ASVs: Theory and experiments," in *Sensing and control for autonomous vehicles: Applications to land, water and air vehicles*. Springer, 2017, pp. 407–431.

[24] R. Skjetne, M. E. N. Sørensen, M. Breivik, S. A. T. Værnø, A. H. Brodtkorb, A. J. Sørensen, K. Kjerstad, V. Calabrò, and B. O. Vinje, "AMOS DP Research Cruise 2016: Academic Full-Scale Testing of Experimental Dynamic Positioning Control Algorithms Onboard R/V Gunnerus," ser. Offshore Mechanics and Arctic Engineering, vol. 1: Offshore Technology, 06 2017.